Continental Shelf Research 29 (2009) 278–291

Contents lists available at ScienceDirect

Continental Shelf Research

journal homepage: www.elsevier.com/locate/csr

A model study of tide- and wind-induced mixing in the Columbia River Estuary and plume

Parker MacCready [a,*], Neil S. Banas [a], Barbara M. Hickey [a], Edward P. Dever [b], Yonggang Liu [a]

[a] University of Washington, Box 355351, Seattle, WA 98195-5351, USA
[b] Oregon State University, USA

ARTICLE INFO

Article history:
Received 5 April 2007
Received in revised form
30 January 2008
Accepted 10 March 2008
Available online 26 March 2008

Keywords:
Mathematical models
River plumes
Estuarine dynamics
Energy budget

ABSTRACT

A numerical simulation of circulation in the Columbia River estuary and plume during the summer of 2004 is used to explore the mixing involved as river water is transformed into shelf water. The model is forced with realistic river flow, tides, wind stress, surface heat flux, and ocean boundary conditions. Simulated currents and water properties on the shelf near the mouth are compared with records from three moorings (all in 72 m of water) and five CTD sections. The model is found to have reasonable skill; statistically significant correlations between observed and modeled surface currents, temperature, and salinity are all 0.42–0.72 for the mooring records. Equations for the tidally averaged, volume-integrated mechanical energy budget (kinetic and potential) are derived, with attention to the effects of: (i) Reynolds averaging, (ii) a time varying volume due to the free surface, and (iii) dissipation very close to the bottom. It is found that convergence of tidal pressure work is the most important forcing term in the estuary. In the far field plume (which has a volume 15 times greater than that of the estuary), the net forcing is weaker than that in the estuary, and may be due to either tidal currents or wind stress depending on the time period considered. These forcings lead to irreversible mixing of the stratification (buoyancy flux) that turns river water into shelf water. This occurs in both the plume and estuary, but appears to be more efficient (17% vs. 5%), and somewhat greater (4.2 MW vs. 3.3 MW), in plume vs. estuary. This demonstrates the importance of both wind and tidal forcing to watermass transformation, and the need to consider the estuary and plume as part of a single system.

1. Introduction

This paper explores the tidally averaged mechanical energy budget within an estuary and coastal river plume. A companion paper (Banas et al., 2008) uses a Lagrangian analysis of this model to address the biologically motivated question of how water upwelled off Washington interacts with the Columbia River (CR) plume. The motivation for the current paper is to better understand how coastal upwelling works in the presence of freshwater input and tidal mixing due to an estuary. Classically, coastal upwelling has been understood as a wind forced process (e.g. Gill, 1982, p. 403; Allen et al., 1995) with alongshore wind stress driving offshore surface Ekman transport and upwelling of deeper waters, particularly in the frictional bottom boundary layer. The addition of a freshwater source may be expected to increase stratification and thus decrease upwelling—because greater energy would be required to lift deep water. Conversely, enhanced tidal currents due to the presence of the estuary may increase vertical turbulent mixing. Thus, from the start it is not clear how the presence of an estuary would affect coastal upwelling. In this paper we do not give a complete answer to the above problem, but instead explore part of it. We focus on just the vertical turbulent mixing in the estuary and river plume, asking whether tides or wind are the more important forcing mechanism in different regions. Not surprisingly, we find that tides dominate in the estuary, while both wind and tides are important in the plume. Interestingly, the net mixing in both places is comparable, indicating that a full understanding of water mass transformation must consider both the estuary and the shelf, and both types of forcing.

This study is part of the RISE project (River Influences on Shelf Ecosystems, www.ocean.washington.edu/rise) funded by US National Science Foundation through the CoOP (Coastal Ocean Processes, www.skio.peachnet.edu/coop/) program. The overall project goal is to understand how coastal biological productivity is affected by a river plume, and early results are given in Orton and Jay (2005), Nash and Moum (2005), Lohan and Bruland (2006), Aguilar-Islas and Bruland (2006), Hickey et al. (2006), Kosro et al. (2006), Kudela et al. (2007) and Pan et al. (2007). The Columbia River is the largest freshwater source on the US west coast south

* Corresponding author. Tel.: +1 206 685 9588; fax: +1 206 543 6073.
E-mail address: parker@ocean.washington.edu (P. MacCready).

0278-4343/$ - see front matter © 2008 Elsevier Ltd. All rights reserved.
doi:10.1016/j.csr.2008.03.015

of the Strait of Juan de Fuca. Monthly average flow (1993–2005, from the USGS station mentioned in Section 2) varies from 9000 $m^3 s^{-1}$ in May to 3500 $m^3 s^{-1}$ in September. The estuarine channel is narrow, being 0.5–5 km wide, and complex—having two main curving channels (Jay and Smith, 1990c; Jay et al., 1988) and a thalweg depth of 15–20 m. Tidal currents are intense, up to 3 m s^{-1} at the surface during ebbs at the mouth. The salt intrusion length varies from 20 to 50 km (Jay and Smith, 1990c). In general, the strong river flow leads to a salt wedge or partially mixed system, but during low flow spring tides it may become well-mixed (Jay and Smith, 1990a, b, c; Jay et al., 1988). Using an extensively instrumented cross-channel section, Hughes and Rattray (1980) found that over half the up-estuary salt flux was due to tidal pumping, with the remainder being due to gravitational circulation. The water leaving the estuary on ebb can have practical salinity of 15 or lower (Jay and Smith, 1990c).

The connection between estuaries and river plumes has been addressed in a number of previous studies. Beardsley and Hart (1978) developed a theoretical model of the stratified (two layer) problem, including an estuarine inflow. Chao and Boicourt (1986) demonstrated how inflowing waters come from beneath the plume in an idealized numerical model. The problem was also studied observationally by Largier (1996) for San Francisco Bay. Garvine (2001) showed how the estuary boundary condition for a shelf plume could profoundly alter the existence of the "bulge" solution. A recent model study of a realistic estuary–plume system is given in Whitney and Garvine (2006).

The region within ~1 tidal excursion of the mouth (say 20 km) will be referred to as the "near field plume." There the plume dynamics are strongly tidal, with a prominent surface front and nonlinear internal wave generation (Nash and Moum, 2005; Orton and Jay, 2005). Farther out on the shelf, the plume is typically 3–20 m thick and loosely identified with surface salinity <31 (Barnes et al., 1972; Landry et al., 1989; Hickey et al., 1998). Ambient seasonal currents and seasonal wind stress tend to push the plume up the length of the Washington coast in winter, and offshore to the southwest in summer (Hickey et al., 2005). Idealized numerical simulations, including the effects of both an ambient current and fluctuating winds, suggest that the plume does not reverse with brief upwelling wind events in winter (Garcia-Berdeal et al., 2002). However in summer, during downwelling favorable wind events, emerging plume water moves north along the Washington coast, so that the plume is commonly bi-directional, with branches north and south of the river mouth (Hickey et al., 2005).

The plume away from the mouth is subject to a variety of types of forcing. Local winds are important in surface boundary layers and in generating alongshelf currents on the shelf. In addition, coastal trapped waves have been shown to be important in the plume region (Battisti and Hickey, 1984). On the inner shelf local wind forcing predominates (Oke et al., 2002). In addition to event scale fluctuations, the Washington–Oregon shelf is subject to southward seasonal mean flow in summer, a baroclinic response to the seasonal large-scale upwelling (Hickey, 1998). Flow on the outer shelf in this region is part of the California Current, flowing southward (Hickey, 1998).

Section 2 describes the model configuration. Model hindcast results for the summer of 2004 are compared with RISE mooring and CTD data in Section 3. In Section 4, the energy equations and their volume integrals are presented. Results are summarized in Section 5.

2. Model configuration

The Columbia is one of the more difficult estuaries to model because of its strong currents, narrow channel and extensive intertidal regions, although significant advances have been made recently using unstructured grids (Zhang et al., 2004; Baptista et al., 2005). Here we use the Regional Ocean Modeling System (ROMS, Rutgers version 2.2) to perform a 3-month hindcast (June–August) of 2004 summertime circulation on the Washington and Oregon shelf, and in the adjoining Columbia River estuary. ROMS (Haidvogel et al., 2000) is widely used for coastal (e.g. Haidvogel, 2005; Peliz et al., 2003) and estuarine (MacCready et al., 2002; Warner et al., 2005b; Li et al., 2005) simulations. The choice of ROMS was motivated by practical concerns. It has a wide user base contributing to the code, has many choices for open boundary conditions, and several different ecosystem models. The model uses a regular finite-difference grid for horizontal discretization, and a generalized "S-coordinate" in the vertical, with 20 elements irregularly spaced between the bottom topography and the free surface (parameters $\theta = 5$, $\theta_b = 0.8$, $h_s = 0$, in the terminology of Haidvogel et al., 2000). The baroclinic time step is 51.75 s, and the barotropic time step is 20 times shorter. The time step is largely constrained by the speed of surface ebb currents at the CR mouth, where the horizontal resolution is finest.

Our simulation uses a stretched, spherical grid (Fig. 1) with ~400 m resolution in the estuary and plume region, telescoping to ~9 km in the far corners. Maximum depth in the domain is 2155 m. The minimum depth is set to 3 m, so wetting and drying of intertidal regions is not included. Bathymetry data are from the GEODAS (Divins and Metzger, 2002) dataset. The model bathymetry is smoothed for numerical accuracy so that the total fractional change in depth over a grid cell is less than 0.8. At 400 m resolution, this still fills in the deeper channels in the Columbia River estuary. To remedy this we artificially deepen the channel along the southern thalweg (the main shipping channel) to match depths from navigational charts. The resulting salt intrusion length is consistent with observations (detailed comparison to be presented in a subsequent paper). The Columbia River beyond about 50 km from the coast is too small to model efficiently with this system, so we add a straight river channel 3 km wide and 3 m deep, extending about 300 km to the east. This allows tidal energy to propagate freely upstream, and almost no tidal energy gets to the eastern edge of the river channel. Experiments with shorter channels produced unrealistic reflection of tidal energy. River flow (Fig. 2a) and temperature are functions of time, taken from daily values at the USGS gauging station 14246900, at Beaver Army Station, 86 km upstream of the mouth (http://waterdata.usgs.gov/or/nwis/dv/?site_no=14246900&agency_cd=USGS). This station represents over 99% of the total flow through the Columbia River mouth during summer (David Jay, personal communication).

Model initial and open boundary values for tracers, subtidal velocity and subtidal surface height come from the Navy Coastal Ocean Model—California Current System (NCOM CCS), which uses extensive data assimilation. NCOM CCS is a higher resolution (~9 km) regional version of the global NCOM model (Barron et al., 2006; Kara et al., 2006). Dynamical open boundary conditions for the free surface and depth-averaged momentum are given by the Chapman (1985) and Flather (1976) formulations. Three-dimensional fields of velocity and tracers are treated with a radiation boundary condition (all as per Marchesiello et al., 2001). Over a six-gridpoint-wide region on the open ocean boundaries the temperature, T, and salinity, s, fields are relaxed to their NCOM CCS values—over 10 days at the boundary and ramping to 60 days at six gridpoints in.

Turbulence closure is given by the $k-\varepsilon$ version of the Generic Length Scale (GLS) formulation (Umlauf and Burchard, 2003) using parameters suggested in Warner et al. (2005a). We used the Canuto A stability functions (Canuto et al., 2001). Minimum values of vertical eddy viscosity and diffusivity were set to 5×10^{-6} $m^2 s^{-1}$. Model sensitivity experiments using the LMD (Large et al. 1994) and MY2.5 (Mellor and Yamada, 1982)

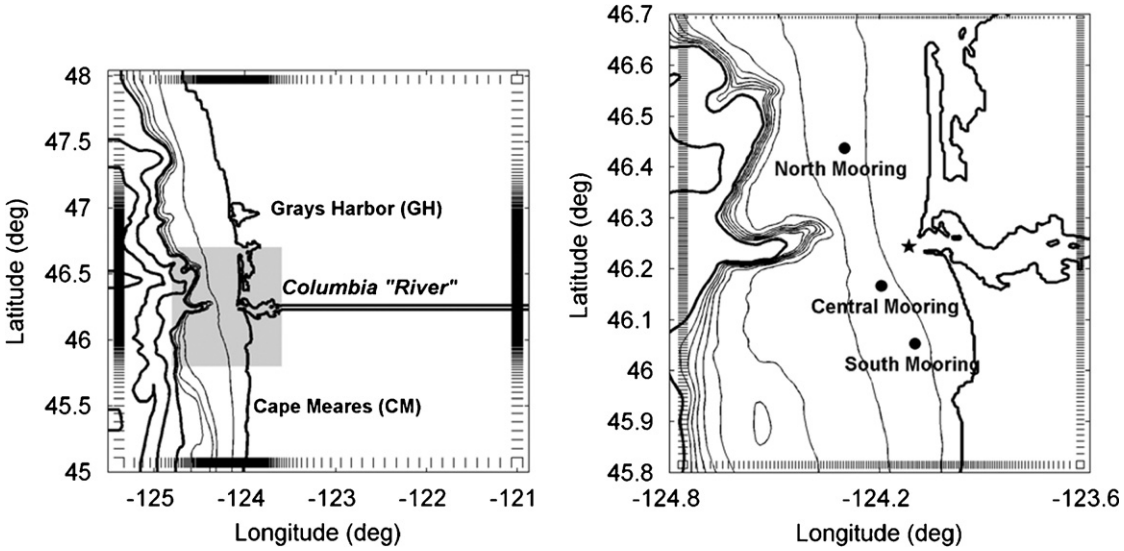

Fig. 1. Left panel: the full domain of the numerical model, which includes the Washington and northern Oregon shelf and slope, and the Columbia River estuary. The resolution of the stretched grid is shown with tick marks at the edges. The Columbia River channel beyond 50 km from the coast is replaced by a straight channel which absorbs tidal energy. Bathymetry contour intervals are 100 m (thin lines) and 500 m (thick lines). The bay to the north of the Columbia River mouth is Willapa Bay. The right panel is a close up of the gray region, showing the locations of three moorings from the 2004 summer RISE program. Thin lines show isobaths on the shelf at 50 m intervals. Grid resolution is ~400 m in this area. The star marks the location of the velocity time series in Fig. 2b.

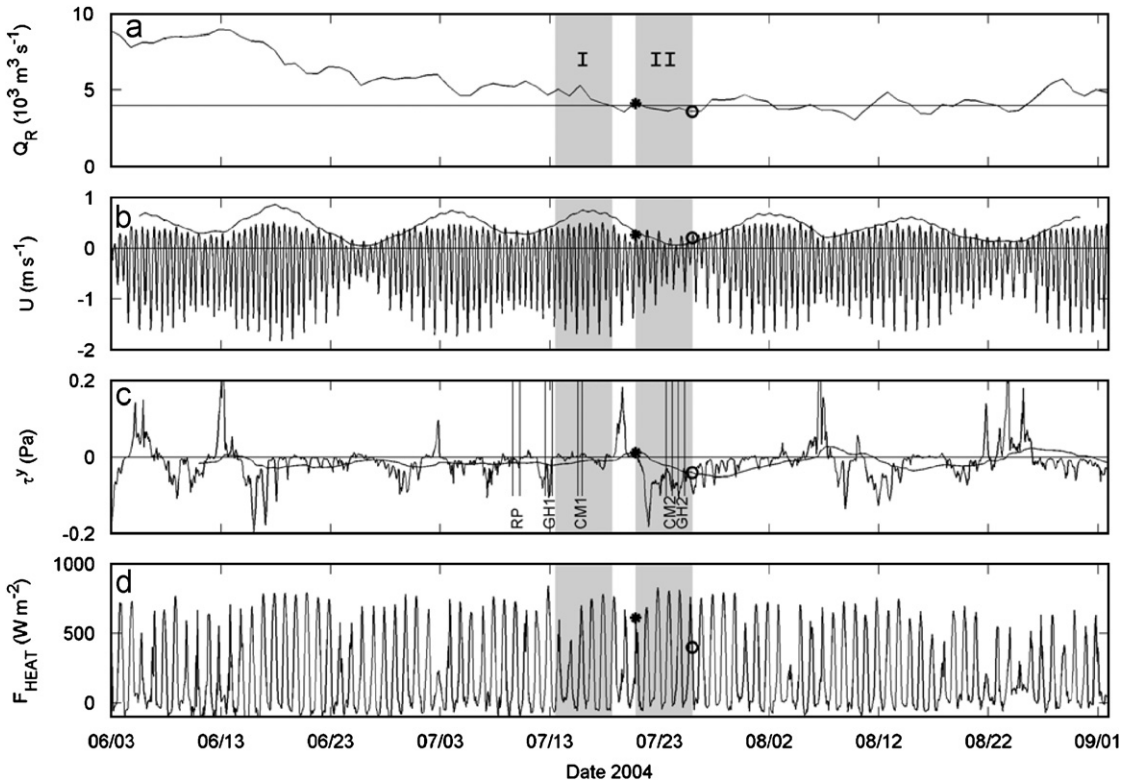

Fig. 2. Time series of model forcing fields during the 3-month simulation period of 2004. Daily river flow is plotted in (a). Time series of E–W depth-averaged model velocity, $\bar{u}$, at the Columbia River estuary mouth (location shown by a star in Fig. 1) is plotted in (b). The smooth line in (b) is the low-pass filtered version of $|\bar{u}|^3$, which is a good indicator of which time periods should be called "spring" or "neap." It has units $m^3 s^{-3}$. Hourly north–south wind stress at the central mooring is plotted in (c), and the timing of CTD sections (Fig. 4) are indicated. The smooth line in (c) is a weighted running average of the previous 8 days of wind stress, where the weighting function is exponential decay toward the past with 8-day e-folding time. Austin and Barth (2002) found this to be a good index of whether or not flow had upwelled on the Oregon shelf. Negative values of stress give rise to upwelling. The net surface heat flux at the central mooring is plotted in (d), where the diurnal cycle is evident. The gray bands in all panels show the two averaging periods for the energy budget. Period I has spring tides and weak winds, while Period II has neap tides and strong upwelling winds. The "*" and "o" indicate times for the panels in Fig. 3 which are nominally downwelled or upwelled according to the Austin and Barth index.

turbulence closures found that overall model skill was greatest using the GLS closure above, particularly in the region of the RISE moorings. Bottom stress is parameterized with a quadratic drag law and a drag coefficient of 3×10^{-3} (e.g. Geyer et al., 2000). A small Laplacian horizontal diffusion of tracers is used, with diffusivity $5\,m^2\,s^{-1}$.

Tidal forcing of surface height and depth averaged velocity at the ocean boundaries is specified using 10 tidal constituents from

the TPXO6.0 analysis (Egbert et al., 1994; Egbert and Erofeeva, 2002). The resulting tidal height on the shelf (e.g. Fig. 9c) is mixed semi-diurnal in character.

Atmospheric forcing comes from the Northwest Modeling Consortium MM5 regional forecast model (Mass et al., 2003). Hourly outputs from their 4 km grid model were archived: 10 m wind, surface pressure, temperature, humidity, and radiation. MM5 model winds were compared with NDBC buoy data in the region of the Columbia River mouth by Tinis et al. (2006). They found that during the summer model mean surface wind direction was within 3° of observations, but was too strong ($3.4\,m\,s^{-1}$ vs. $2.7\,m\,s^{-1}$). For our simulation period, the time mean wind stress at the central mooring (Fig. 1) was 0.0195 Pa, 79% higher than the 0.0109 Pa observed by an anemometer on that mooring. In addition, the model mean wind stress was rotated 15° counterclockwise relative to observations. However, the mean is small compared to the important windstress events, which have magnitudes on the order of 0.05–0.1 Pa. Correlation is discussed in more detail in relation to Fig. 8. Surface fluxes of momentum and heat are calculated in ROMS using bulk formulations (Fairall et al., 1996a, b; Liu et al., 1979). Net shortwave radiation and downward longwave radiation are given as external forcing, and then upward longwave, sensible, and latent heat fluxes are calculated in the model. Time series of wind stress and heat flux at the central mooring are plotted in Fig. 2c and d. Periods of downwelling and upwelling winds are evident, particularly during July 20–26, one of the periods we will focus on for our energy analysis. Evaporation and precipitation (as they affect salinity) were set to zero, because during summer they have negligible effect on surface salinity when compared with the Columbia River.

Model sensitivity experiments (to be presented in a separate paper) demonstrate that the model is sensitive to different parameter choices. Experiments with different "Jerlov water types" (which governs the penetration depth of short wave radiation) indicate that water types 1 and 3 result in a warmer water temperature in the subsurface layer and a cooler surface temperature, and water type 5 (smallest penetration distance, used here) gives a temperature distribution that has the best agreement with the observations. Experiments on the nudging within the six-grid points of the open boundaries show that nudging is necessary for this model domain. Nudging of different variables has different improvements in model skill, with the best result found to be from complete nudging (nudging of all the available variables: tracers, 2D and 3D momentum) that we use here.

3. Comparisons with observations

In this section, selected aspects of the simulated circulation and stratification are compared with observations. The goal is to illustrate what the model does well, and what it does poorly. Typical model salinity fields are shown in Fig. 3 for the downwelled and upwelled conditions whose times are denoted

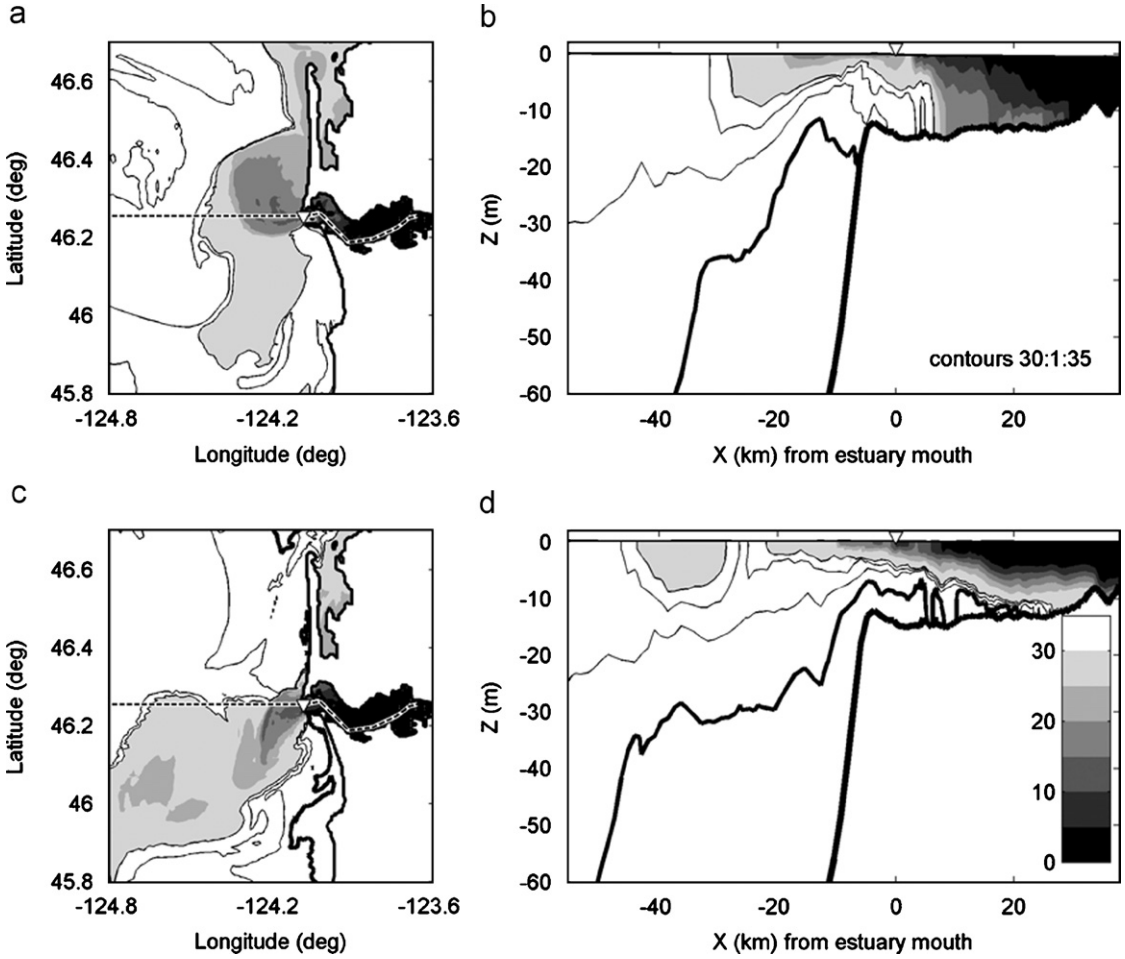

Fig. 3. Model plume response to an upwelling event. Surface salinity at the end of a downwelling event (time "*" in Fig. 2, July 20, 2004, 20:51 GMT) is plotted in (a), and after ~5 days of upwelling winds in (c) (time "o" in Fig. 2, July 26, 2004, 00:01 GMT). Corresponding salinity sections on the dashed line are plotted in (b) and (d). The thick contour is $s = 33$.

by "*" and "o" in Fig. 2. As expected, downwelling winds cause the emerging plume to turn north along the Washington coast. Upwelling winds push both the emerging new plume and the aged plume to the southwest, the offshore drift being caused by Ekman transport. The effect of upwelling is also evident in the sections, with the 33 isohaline rising into the estuary.

Fig. 4 compares cross-shelf salinity sections on the RP (river plume axis) GH (Grays Harbor) and CM (Cape Meares) lines during weak wind and upwelling periods (times indicated in Fig. 2c and locations in Fig. 4a). There is a long history of observations at or near the GH line (Landry et al., 1989). The observations, from CTD sections made by the R/V *Wecoma*, show evidence of low salinity plume water in the upper 10 m, and the strong upward tilt of isohalines on the shelf. On the plume axis (Fig. 4b) the model does a good job predicting the salinity field, except that it is too fresh by about 4 in the upper 3 m. On the cross-shelf sections (Fig. 4c–f) the model reproduces the main features of the salinity field, such as the shoaling of the 33 isohaline toward shore, and the plume stratification near the surface. The most salient difference is that the model salinity at depth is too high by about 0.5 at the most offshore stations on the CM line.

We make more quantitative comparisons with the three mooring records (locations shown in Fig. 1). The analysis here loosely follows that of Oke et al. (2002). The three mooring were all very near the 72 m isobath (Fig. 1), and were positioned primarily to resolve variation of the CR plume structure on that isobath. Each had a 300 kHz ADCP (Teledyne RD Instruments) looking downward from the toroidal surface buoy (7.5 min ensembles, 0.5 m bins). Temperature and salinity were measured by Seacats (Sea-Bird electronics, Inc.) at depths of 1 m (in the buoy), 5 m, and 20 m (3.75 min samples). Bottom pressure was measured on the anchor (4 min samples), and wind velocity was

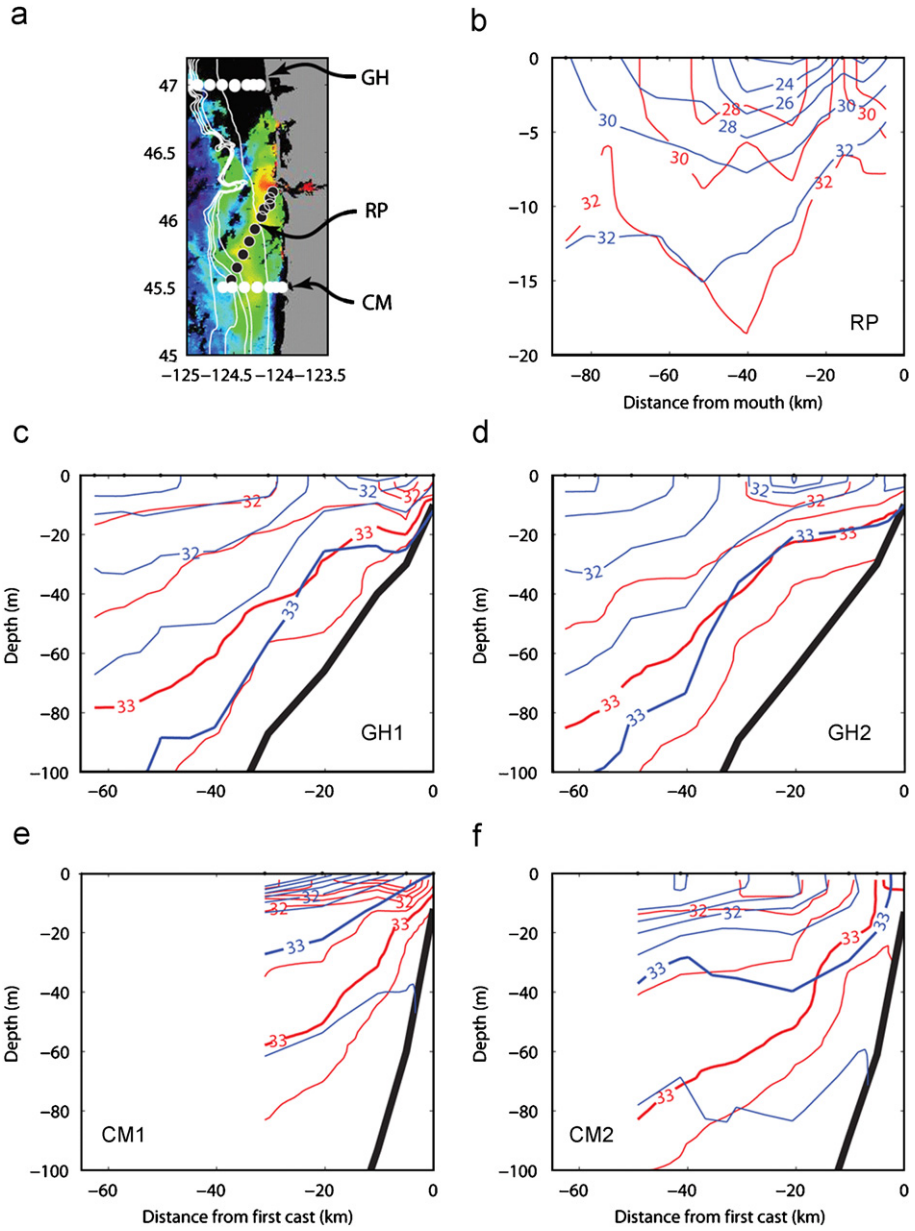

Fig. 4. Comparison of observed (red lines) and modeled (blue lines) salinity from five CTD sections on the plume axis (RP), Grays Harbor (GH1 and GH2), and Cape Meares (CM1 and CM2) lines. Times are shown in Fig. 2c. The contour interval is 2 on the RP section, and 0.5 on all others. The $s = 33$ isohaline is thick in all cases. A MODIS satellite turbidity image is shown in (a) with yellow to red indicating the high turbidity presumably associated with the Columbia River plume. Location of a ship CTD section down the observed plume axis three days earlier is shown as black dots in (a), and the salinity section on this path (RP) is plotted in (b). Salinity sections on the GH and CM lines are plotted in (c)–(f), with station locations shown as white dots in (a). Satellite images courtesy of Raphael Kudela, UCSC (http://oceandatacenter.ucsc.edu/RISE/).

measured by an anemometer on the buoy at 3 m height (1 min samples). All records were hourly averaged and model output was interpolated to the same time axis. In general, observational errors are small compared with errors between the observations and the model.

Focusing on record-mean properties vs. depth for the central mooring, which is most directly affected by the river plume, Fig. 5, the results are reasonably encouraging. Time-mean velocity Fig. 5a and d matches well in both magnitude and vertical structure. The standard deviation of the horizontal velocities, Fig. 5b, and e, are consistently underpredicted by the model, but still show the strong surface enhancement evident in the observations. The temporal correlation of the velocities, Fig. 5c and f, is also reasonable, averaging over 0.45 where the estimate is significant. The correlation coefficient between a model time series, m, and an observed time series, o, both of length N (the number of values), is given by (e.g. Oke et al., 2002)

$$CC = \frac{1}{N}\sum_{i=1}^{N}\frac{(m_i - \bar{m})(o_i - \bar{o})}{(S_m S_o)}, \tag{3.1}$$

where m_i and o_i are the ith values of the time series, which have means $\bar{m}$ and $\bar{o}$ and standard deviations S_m and S_o, respectively. The confidence level for significance is calculated as per Emery and Thomson (1997, Appendix E). We calculate degrees of freedom (DOF) as $DOF = N' - 2$, where N' is the record length divided by the time of the first zero crossing of the lagged autocorrelation function for a given low-passed observational record.

Mean temperature and salinity values in the top 20 m, Fig. 5g and h, match reasonably well with observations, but average ~1 ° fresh and 1 °C cool at the surface. Similar comparisons at the north and south moorings are somewhat worse, showing excess southward flow of ~10 cm s^{-1} at all depths at the north (Fig. 6d), and significant underprediction of the meridional current standard deviation (Figs. 6e and 7e). The surface water at the north mooring is also noticeably too salty (Fig. 6g). The discrepancies at the north mooring appear to be caused by the model underpredicting the amount of time that the plume was present at the mooring. The general underprediction of the current standard deviation may be due to the lack of internal waves in the open boundary conditions, but we have no way to test this.

Next we consider low pass filtered (40 h Hanning window) time series at the central mooring. The low-passed along shelf current (Fig. 8a) at 3 m depth matches the observations at times, but also has significant mismatches, e.g. in mid-July. The mismatch exists despite the close agreement between observed and modeled wind stress (Fig. 8f). The correlation is 0.63, and is significant at the 95% confidence level. Low-passed cross-shelf currents (Fig. 8b) at 3 m are weaker and less well-correlated ($CC = 0.45$, not significant at 95%). In Oke et al. (2002), it was found that currents in 50 m of water on the Oregon shelf were more strongly forced by local winds, and compared better with the model, than those in 80 m depth (our moorings are at the 72 m isobath). The mismatch in deeper water was attributed to the absence of an along-shelf pressure gradient and associated currents in Oke et al. (2002). This large scale forcing, which may

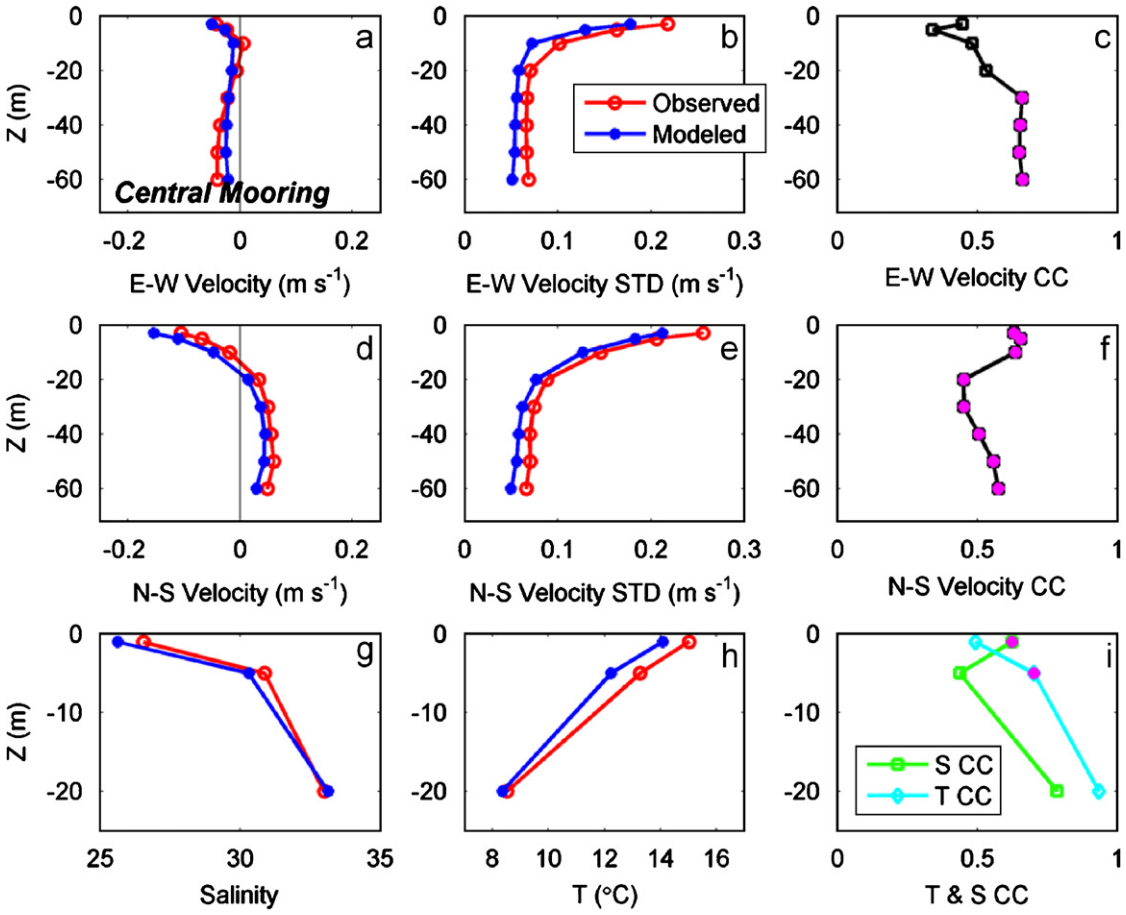

Fig. 5. Comparison of hourly modeled and observed properties from the central mooring, all for the period June 22 to September 1, 2004. Time-mean velocities vs. depth are plotted in (a) and (d). The standard deviation of the currents is plotted in (b) and (e), and the correlation coefficient (CC) between hourly observed and modeled values is plotted in (c) and (f). Time-mean salinity and temperature at three depths are plotted in (g) and (h), with CC shown in (i). Correlation coefficients significant at 95% confidence are marked magenta.

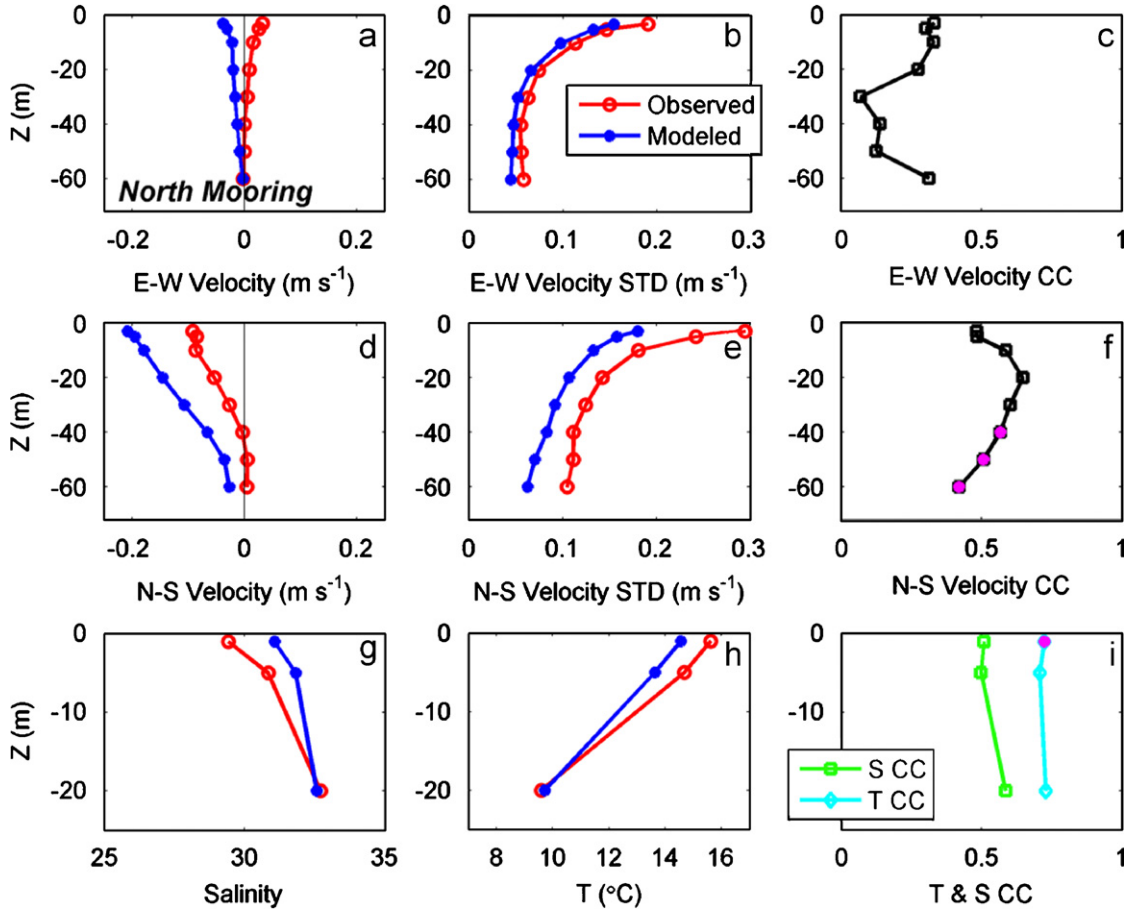

Fig. 6. Comparison of hourly modeled and observed properties from the north mooring, all for the period June 22 to September 1, 2004. Time-mean velocities vs. depth are plotted in (a) and (d). The standard deviation of the currents is plotted in (b) and (e), and the correlation coefficient (CC) between hourly observed and modeled values is plotted in (c) and (f). Time-mean salinity and temperature at three depths are plotted in (g) and (h), with CC shown in (i). Correlation coefficients significant at 95% confidence are marked magenta.

be due to remotely forced coastal trapped waves (Battisti and Hickey, 1984) is in principle included in our boundary forcing from the NCOM CCS model. Near surface salinity (Fig. 8c, $CC \approx 0.62$, significant at 95%) and salinity stratification (Fig. 8e, $CC = 0.61$, significant at 95%) show reasonable skill in the model. The model near-surface temperature is occasionally too warm near the surface (Fig. 8d).

High-passed time series at the central mooring are presented in Fig. 9. In general, tidal currents near the surface (Fig. 9a) are under-predicted by the model, resulting in the decreased standard deviation evident in Fig. 5e. As stated above, the reasons for this difference are not known. High-passed near-surface salinity (Fig. 9b) has a similar character in model and observations but the correlation is low. Comparing high-passed model surface height with that calculated from a bottom pressure sensor at the central mooring (Fig. 9c) shows that the model tidal forcing is basically correct ($CC = 0.94$), although not as finely tuned as the Chesapeake model of Zhong and Li (2006). Finally, the high-passed along-shelf wind stress has significant energy in the diurnal band, and this is also present in the model forcing (Fig. 9d).

4. Energy integrals

The model-data comparisons give modest confidence in the model. It is not grossly misrepresenting broad features of the shelf and plume currents and hydrography. Now we will use the model to estimate the relative importance of tide- and wind-forced mixing to the process of turning river water into ocean water. To do this we will calculate tidally averaged integrals of terms in the mechanical energy equation over two different geographical regions (estuary and plume). Averages will be made over two contrasting time periods, identified in Fig. 2. Period I has spring tides and relatively weak winds, whereas Period II has neap tides and strong upwelling winds. Each is 10 M_2 tidal periods long.

Energy has been used as an organizing principle in a limited number of estuarine studies in the past. Considering tidal energy at the global scale (Munk, 1997; Munk and Wunsch, 1998) is it estimated that about 3.5 TW of energy is input to the tides by the sun and moon. The majority of this, 2.6 TW, is dissipated in the shallow coastal ocean. Those authors estimate that only about 4% of this, 0.1 TW, goes into "perforations" such as bays, inlets, fjords and estuaries. A maximum of ~20% of this is thought to be available for irreversible mixing of the stratification (buoyancy flux). In studies of fjord energetics, Stigebrandt and Aure (1989) have estimated this efficiency to be closer to 5%, presumably because much of the dissipation occurs in unstratified regions. Changes in vertically integrated potential energy have long been used (Simpson et al., 1990) as a way of understanding estuarine function. A number of studies have calculated barotropic tidal energy flux in real estuaries, and calculated net dissipation as either the divergence of this flux (Lavelle et al., 1988), or directly from numerically simulated shears (Zhong and Li, 2006, which also contains an excellent introduction to the literature). An important step taken by Weisberg and Zheng (2003) was to

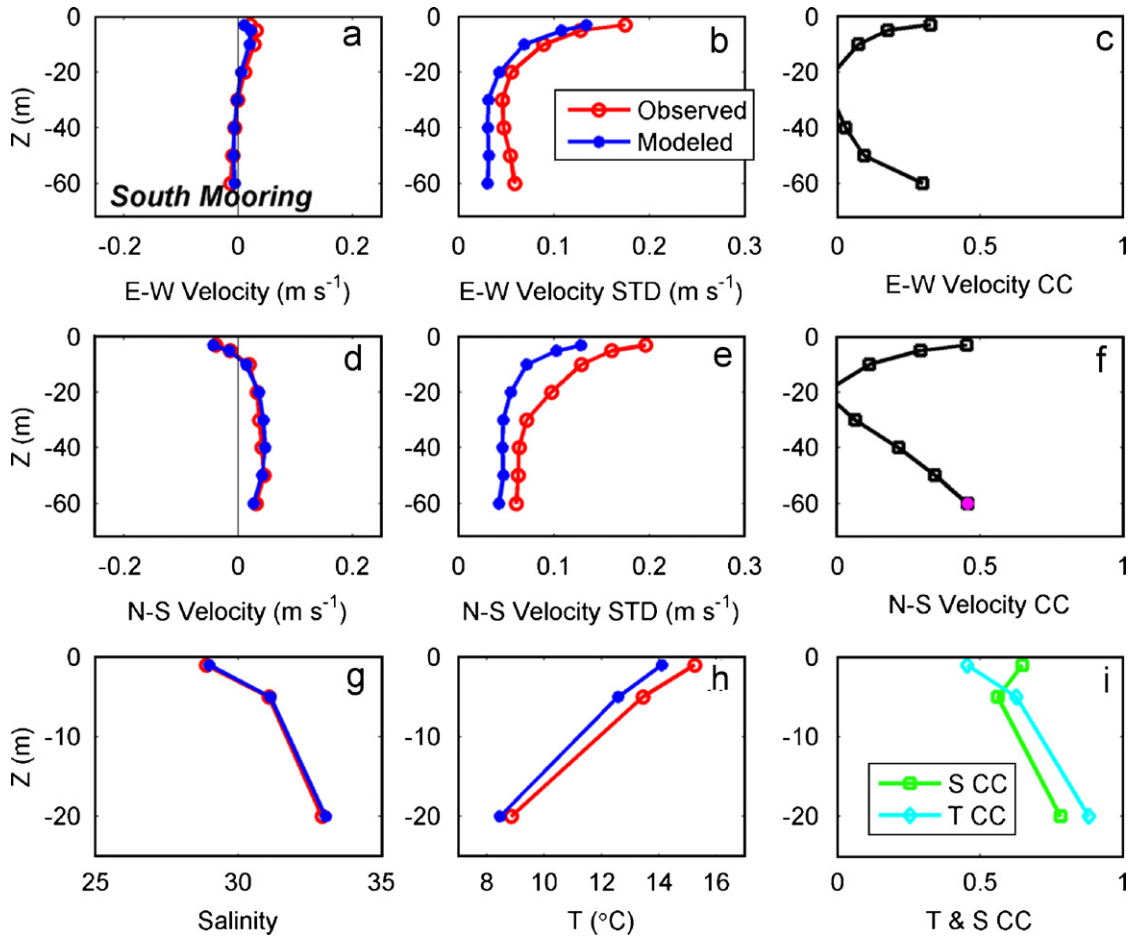

Fig. 7. Comparison of hourly modeled and observed properties from the south mooring, all for the period June 22 to September 1, 2004. Time-mean velocities vs. depth are plotted in (a) and (d). The standard deviation of the currents is plotted in (b) and (e), and the correlation coefficient (CC) between hourly observed and modeled values is plotted in (c) and (f). Time-mean salinity and temperature at three depths are plotted in (g) and (h), with CC shown in (i). Correlation coefficients significant at 95% confidence are marked magenta.

compute all terms in the volume integrated energy budget, in their case for a numerical model of Charlotte Harbor. They used this method to explore how mixing affects the tidally averaged exchange flow.

We will derive the necessary equations and their volume integrals here, noting some differences with previous derivations. We begin with the Boussinesq, Reynolds averaged equations for momentum, incompressibility, and density:

$$\frac{D\mathbf{u}}{Dt} + f\hat{k} \times \mathbf{u} = -\frac{1}{\rho_0}\nabla p - \frac{\hat{k}g\rho}{\rho_0} + \nabla \cdot (K_M \nabla \mathbf{u}), \tag{4.1}$$

$$\nabla \cdot \mathbf{u} = 0, \tag{4.2}$$

$$\frac{D\rho}{Dt} = \nabla \cdot (K_D \nabla \rho), \tag{4.3}$$

The velocity vector is $\mathbf{u} \equiv (u, v, w)$, and Eq. (4.1) is a vector equation. $D(\,)/Dt \equiv \partial(\,)/\partial t + \mathbf{u} \cdot \nabla$ is the material derivative, f is the Coriolis frequency, $\hat{k}$ is the vertical unit vector, ρ_0 a constant background density ($1025\,\mathrm{kg\,m^{-3}}$), and ρ is the full density. K_M is the eddy viscosity and K_D is the eddy diffusivity. The pressure, p, is assumed hydrostatic, so that

$$p = p_{00} + [p_{BT}] + \{p_{BC}\} = -\rho_0 g z + [\rho_0 g \eta_{BT}] + \left\{\rho_0 g \eta_{BC} + \int_z^{\eta} g\rho'\,dz\right\}, \tag{4.4}$$

where $\rho' \equiv \rho - \rho_0$ and the free surface is at $\eta = \eta_{BT} + \eta_{BC}$. The dynamically active pressure has been divided into barotropic, p_{BT}, and baroclinic, p_{BC}, portions following the method of Nash et al. (2005). This distributes the pressure due to surface height elevation between barotropic and baroclinic parts such that the vertical average of p_{BC} is zero. The pressure is defined as the actual pressure minus atmospheric pressure (assumed constant), so $p = 0$ at $z = \eta$. The use of hydrostatic pressure is formally inconsistent with Eq. (4.1) in which the full vertical momentum equation is used. We retain the Dw/Dt terms in the derivation below for theoretical convenience, but these are negligibly small. The vertical velocity is also not included in the calculation of kinetic energy from model fields, again because it makes only a negligible contribution.

We form equations for kinetic energy per unit volume, $KE_V \equiv (1/2)\rho_0 \mathbf{u} \cdot \mathbf{u}$, and potential energy per unit volume, $PE_V \equiv \rho g z$, by taking $\rho_0 \mathbf{u} \cdot$ (Eq. (4.1)) and gz (Eq. (4.3)), which give

$$\begin{aligned}\frac{D}{Dt}(KE_V) &= -\nabla \cdot (p\mathbf{u}) - \rho g w + \nabla \cdot (\rho_0 K_M \mathbf{u} \cdot \nabla \mathbf{u}) \\ &\quad - \rho_0 K_M (\nabla \mathbf{u})^2, \\ &= -\nabla \cdot (p\mathbf{u}) - \rho g w + \frac{\partial}{\partial x_j}\left(u_i \rho_0 K_M \frac{\partial u_i}{\partial x_j}\right) \\ &\quad - \rho_0 K_M \left(\frac{\partial u_i}{\partial x_j}\right)^2,\end{aligned} \tag{4.5}$$

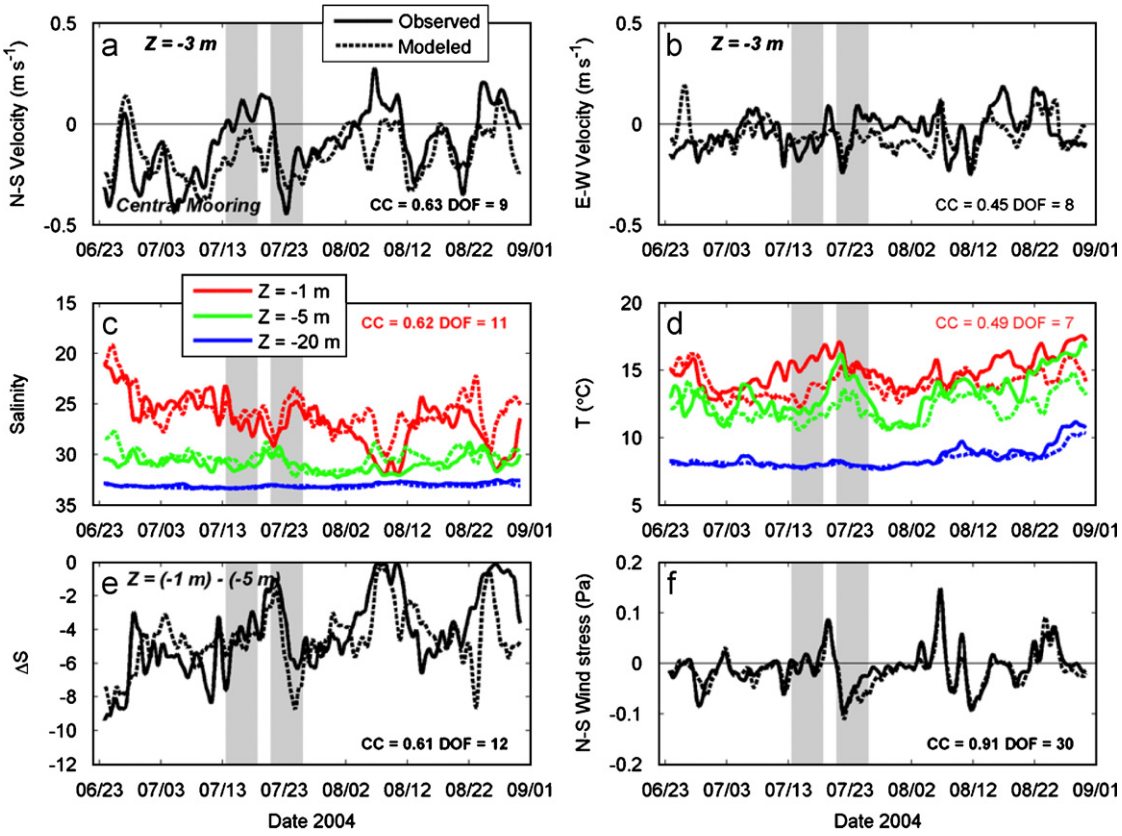

Fig. 8. Comparison of observed and modeled low pass filtered (40 h) time series from the central mooring. North–south and east–west currents are plotted in (a) and (b). Salinity and temperature at three depths below the surface are plotted in (c) and (d). The near-surface stratification in s is plotted in (e). North–south wind stress is plotted in (f). For all panels, the correlation coefficient (CC) is shown as well as the degrees of freedom (DOF) of the low-passed observed signal; in (c) and (d) the CC is for the shallowest ($z = -1$ m) record. *CC* values in (a), (c), (e), and (f) are significant at the 95% confidence level. Gray bands show energy analysis Periods I and II.

$$\frac{D}{Dt}(PE_V) = \rho g w + \nabla\cdot(gzK_D\nabla\rho) - gK_D\frac{\partial\rho}{\partial z}. \tag{4.6}$$

Note that we have given an alternative version of the RHS of Eq. (4.5) using indicial notation (Kundu and Cohen, 2002, p. 24–32) where it clarifies operations in the viscous terms. These equations differ from those given in Weisberg and Zheng (2003) and Zhong and Li (2006) in that we include multiplication by w in the formation of the kinetic energy equation, which thus retains the $KE \leftrightarrow PE$ conversion term $\rho g w$ (see Gill, 1982, pp. 76–82; Winters et al., 1995; Wunsch and Ferrari, 2004). Our *PE* equation differs from the treatments in Gill (1982), Winters et al. (1995), and Wunsch and Ferrari (2004) in that we begin with a Reynolds averaged density Eq. (4.3), which gives rise to the explicit eddy diffusion terms in Eq. (4.6). Physically, Eq. (4.6) is identical to Eq. (12) in Wunsch and Ferrari (2004) but with the Reynolds averaged conversion term, as in their Eq. (23).

Next we take volume integrals of the above equations, over an arbitrary geographical region that may have open vertical sides with area A_{OPEN}, and which extends from the sea floor (area A_{BOT}) to the sea surface (area A_{TOP}), both of which are irregular surfaces. The vertical projection of the volume has area A_0. Calculation of the volume integral terms in Eqs. (4.5) and (4.6) are straightforward, with the exception of the material derivative, because the shape of the volume changes as the free surface moves. This may be treated in the following way. Note that for an arbitrary scalar, φ:

$$\frac{D\varphi}{Dt} = \frac{\partial\varphi}{\partial t} + \mathbf{u}\cdot\nabla\varphi = \frac{\partial\varphi}{\partial t} + \nabla\cdot(\mathbf{u}\varphi), \tag{4.7}$$

where we have made use of Eq. (4.2). The Generalized Leibniz' Theorem (Kundu and Cohen, 2002, Chap. 4) states that

$$\frac{\mathrm{d}}{\mathrm{d}t}\int_V \varphi\,\mathrm{d}V = \int_V \frac{\partial\varphi}{\partial t}\,\mathrm{d}V + \int_A \varphi u_A\,\mathrm{d}A, \tag{4.8}$$

where A is the bounding area of volume V, with outward normal $\hat{n}$, and the bounding area of the volume may be moving with outward normal speed u_A. Then, taking the volume integral of Eq. (4.7) and combining with Eq. (4.8), we find the general expression:

$$\int_V \frac{D\varphi}{Dt}\,\mathrm{d}V = \frac{\mathrm{d}}{\mathrm{d}t}\int_V \varphi\,\mathrm{d}V + \int_A \varphi(\mathbf{u}\cdot\hat{n} - u_A)\,\mathrm{d}A. \tag{4.9}$$

For the volume considered in this paper, note that on A_{OPEN} and on A_{BOT} we have $u_A = 0$ because these boundaries are not moving, and on A_{TOP} the normal fluid velocity is identical to that of the boundary, so $(\mathbf{u}\cdot\hat{n} - u_A) = 0$. Thus, we are left with

$$\int_V \frac{D\varphi}{Dt}\,\mathrm{d}V = \frac{\mathrm{d}}{\mathrm{d}t}\int_V \varphi\,\mathrm{d}V + \int_{A_{\mathrm{OPEN}}} \varphi\mathbf{u}\cdot\hat{n}\,\mathrm{d}A. \tag{4.10}$$

This expression, along with Gauss' Divergence Theorem, $\int_V \nabla\cdot\mathbf{C}\,\mathrm{d}V = \int_A \mathbf{C}\cdot\hat{n}\,\mathrm{d}A$ for an arbitrary vector field $\mathbf{C}$, allows us to form volume integrals of Eqs. (4.5) and (4.6). These are:

$$\begin{aligned}\frac{\mathrm{d}}{\mathrm{d}t}\int_V KE_V\,\mathrm{d}V + \int_{A_{\mathrm{OPEN}}} KE_V u_n\,\mathrm{d}A &= -\int_{A_{\mathrm{OPEN}}} pu_n\,\mathrm{d}A \\ &- \int_V \rho g w\,\mathrm{d}V + \int_{A_0}(u\tau^x + v\tau^y)|_{z=\eta}\,\mathrm{d}A \\ &- \int_V \rho_0 K_M(u_z^2 + v_z^2)\,\mathrm{d}V\end{aligned} \tag{4.11}$$

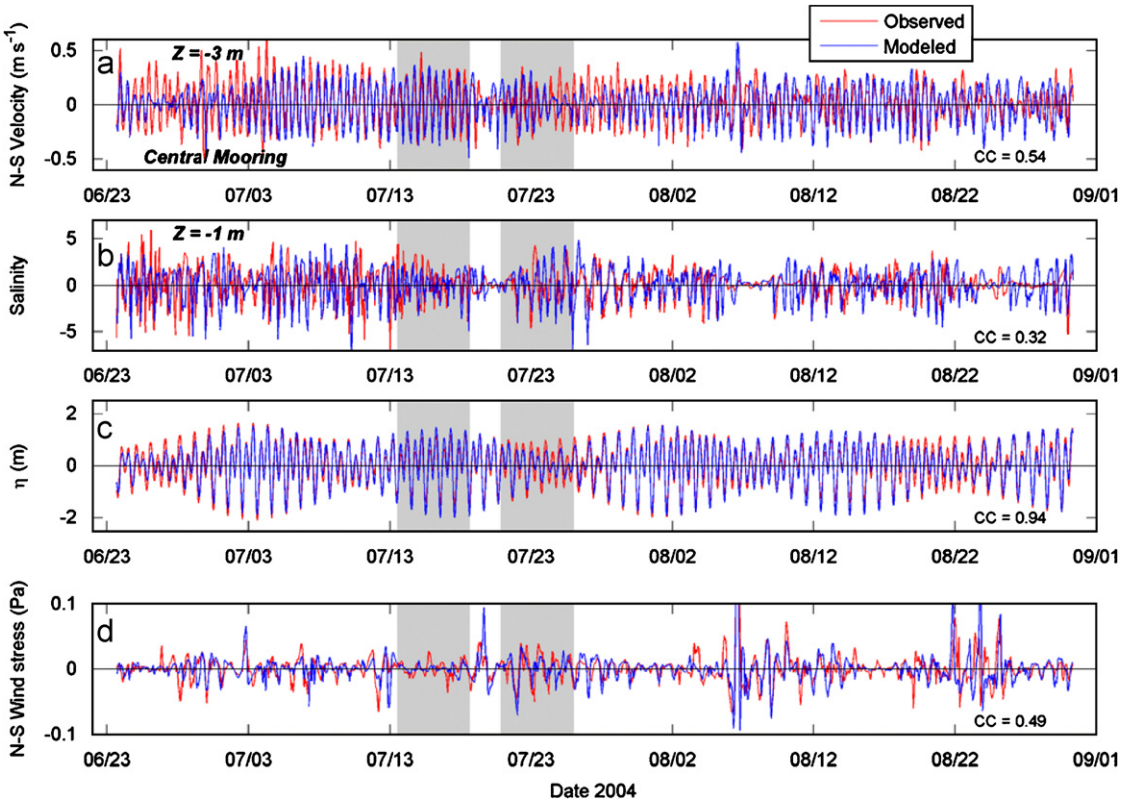

Fig. 9. Comparison of observed (red) and modeled (blue) high pass filtered time series from the central mooring. North–south currents are plotted in (a), showing a predominantly tidal signal. Salinity at 1 m below the surface, (b), also has large tidal variance, except when downwelling winds push the plume to the north so it misses the mooring, as seen around July 20. Tidal height from the model and that estimated from a bottom pressure sensor on the central mooring are plotted in (c). High-passed north–south wind stress is plotted in (d), showing a strong diurnal signal. Gray bands show energy analysis Periods I and II.

and

$$\frac{\mathrm{d}}{\mathrm{d}t}\int_V PE_V\,\mathrm{d}V + \int_{A_{\mathrm{OPEN}}} PE_V u_n\,\mathrm{d}A = \int_V \rho g w\,\mathrm{d}V + \int_{A_0}\left(g\eta K_D\frac{\partial\rho}{\partial z}\right)\Big|_{z=\eta}\mathrm{d}A - \int_V gK_D\frac{\partial\rho}{\partial z}\,\mathrm{d}V, \tag{4.12}$$

where $u_n \equiv \mathbf{u}\cdot\hat{n}$. The second-to-last term in Eq. (4.11) involves the wind stress vector (τ^x, τ^y), and we have assumed $\mathbf{u} = 0$ on A_{BOT} (the "no-slip" condition). In the last term of Eq. (4.11), it is assumed that the shear is dominated by the vertical shear of horizontal currents (the subscript z is a partial derivative).

Using the definition $\rho = \rho_0 + \rho'$, and the hydrostatic pressure, Eq. (4.4), it may be shown that the large term $\int_{A_{\mathrm{OPEN}}} \rho_0 g z u_n\,\mathrm{d}A$ appears on the RHS of Eq. (4.11) as part of the pressure work term (due to p_{00}), and on the LHS of Eq. (4.12) as part of the PE_V advection term, and so it will cancel out when we add the two. We may also note that

$$\int_V \rho_0 g z\,\mathrm{d}V = \int_{A_0}\frac{1}{2}\rho_0 g z^2|_\zeta^\eta\,\mathrm{d}A = \int_{A_0}\frac{1}{2}\rho_0 g(\eta^2-\zeta^2)\,\mathrm{d}A, \tag{4.13}$$

where the bottom is at $z = \zeta$. Using the time-derivative of this, we may add Eq. (4.11) to Eq. (4.12) to find the desired volume-integrated mechanical energy budget:

$$\underbrace{\frac{\mathrm{d}}{\mathrm{d}t}\int_V KE_V\,\mathrm{d}V}_{KE\ STORAGE} + \underbrace{\frac{\mathrm{d}}{\mathrm{d}t}\int_{A_0}\frac{1}{2}\rho_0 g\eta^2\,\mathrm{d}A}_{PE_0\ STORAGE} + \underbrace{\frac{\mathrm{d}}{\mathrm{d}t}\int_V \rho' g z\,\mathrm{d}V}_{PE_1\ STORAGE} = \underbrace{-\int_{A_{OPEN}}(KE_V+\rho' g z)u_n\,\mathrm{d}A}_{KE\ ADV+PE_1\ ADV} \underbrace{-\int_{A_{OPEN}}(p_{BT}+p_{BC})u_n\,\mathrm{d}A}_{PW_0+PW_1}$$
$$\underbrace{+\int_{A_0}(u\tau^x+v\tau^y)|_{z=\eta}\,\mathrm{d}A}_{WIND} \underbrace{-\int_V \rho_0 K_M(u_z^2+v_z^2)\,\mathrm{d}V}_{DISS} \underbrace{-\int_V gK_D\frac{\partial\rho}{\partial z}\,\mathrm{d}V}_{BUOY}. \tag{4.14}$$

We have neglected the surface buoyancy flux term, which makes a negligible contribution when the average sea surface height is around $z = 0$. We have given names to the individual terms: *ADV* stands for advection, *PW* is for pressure work, *DISS* is for dissipation, *BUOY* is the buoyancy flux, and subscripts 0 and 1 refer nominally to barotropic and baroclinic terms, respectively. We will be considering an average of this budget over many tidal cycles, and may reasonably expect the storage terms to be small. Then the main *forcing* terms are expected to be PW_0, the convergence of barotropic (presumably tidal) pressure work, and *WIND*. The main energy *sink* is the (negative definite) term *DISS*, which is *TKE* production in the turbulent energy budget. Some fraction (<20%) of this may end up in the (positive definite) irreversible mixing of the stratification, *BUOY*. The contribution of the remaining pressure work and advection terms is less certain, because of the large open boundaries of our volume.

The actual integration of DISS is complicated by the strong shears and intense dissipation just above the bottom boundary. Numerically, we may separate the volume integral DISS into two parts:

$$\underbrace{-\int_V \rho_0 K_M(u_z^2+v_z^2)\,\mathrm{d}V}_{DISS} = \underbrace{-\int_{A_0}\left[\int_\zeta^{z'}\rho_0 K_M(u_z^2+v_z^2)\,\mathrm{d}z\right]\mathrm{d}A}_{DISS_{BOT}} \underbrace{-\int_{A_0}\left[\int_{z'}^{\eta}\rho_0 K_M(u_z^2+v_z^2)\,\mathrm{d}z\right]\mathrm{d}A}_{DISS_{INT}}, \tag{4.15}$$

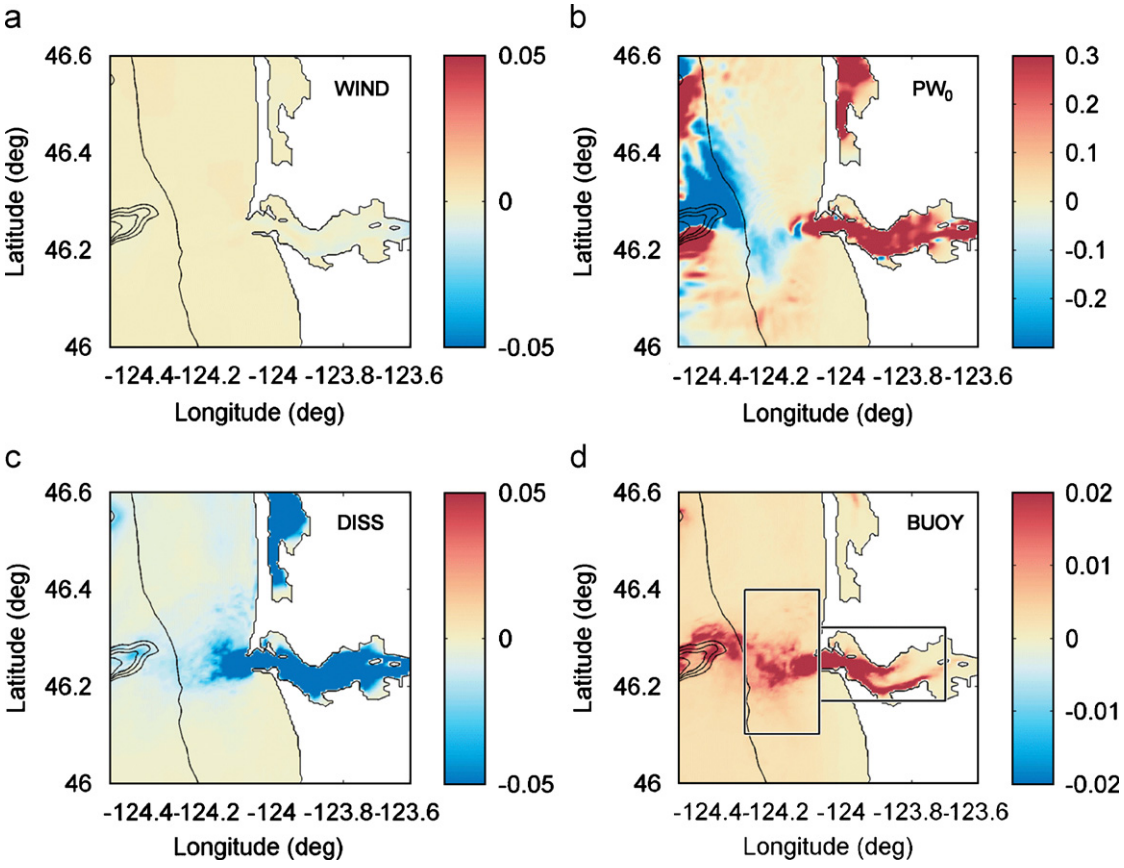

Fig. 10. Selected fields from the time-averaged, vertically integrated, mechanical energy budget, all with units Wm^{-2}. These are averaged over the spring tide, weak wind Period I indicated in Fig. 2. The wind stress term is plotted in (a). All variable names are as given in Eq. (4.14). The tidal pressure work convergence term is plotted in (b). Dissipation and buoyancy flux are plotted in (c) and (d). Isobaths are contoured every 100 m. The "plume" and "estuary" regions for volume integration are indicated by boxes in (d).

where z' is the z-position of the first model velocity grid point above the bottom. The interior portion of the dissipation, $DISS_{INT}$, is readily calculated from model fields. The portion below the bottom gridpoint is more difficult because of the rapid changes in velocity and diffusivity. However, if we assume that z' is well within the bottom log layer, then the shear stress is approximately equal to the bottom stress anywhere from the bottom to z' (e.g. for flow only in the x-direction):

$$\rho_0 K_M u_z|_{z\leqslant z'} \cong \rho_0 C_D u|u|_{z=z'}. \tag{4.16}$$

We may also approximate the shear in this region as being linear:

$$\frac{\partial u}{\partial z} \cong \frac{u(z=z')}{z'-\zeta}. \tag{4.17}$$

Using these, $DISS_{BOT}$ may be evaluated directly as:

$$DISS_{BOT} = -\int_{A_0}\left[\int_{\zeta}^{z'} \rho_0 K_M(u_z^2+v_z^2)\,\mathrm{d}z\right]\mathrm{d}A \cong -\rho_0 C_D|\mathbf{u}_H|^3_{z=z'}, \tag{4.18}$$

where $\mathbf{u}_H=(u,v)$. Expression (4.18) is identical to the bottom dissipation term given in Weisberg and Zheng (2003), their Eq. (9) and Zhong and Li (2006), their Eq. (B9). However, in their case, they assume a non-zero bottom velocity. Here we have shown that the same expression arises from a no-slip boundary condition as a portion of the interior dissipation.

We average all the terms in Eq. (4.14) over two time intervals, each 10 M_2 tidal periods in length (using model saves every lunar hour, or 3726 s): Period I has spring tide with weak winds, and Period II has neap tide with strong upwelling winds. Selected terms are plotted in Fig. 10 (Period I) and Fig. 11 (Period II), shown as integrals over each horizontal grid cell, so these are effectively vertically integrated terms. We present only the forcing terms (PW_0 and *WIND*) and the turbulent dissipation and mixing terms (*DISS* and *BUOY*). The wind forcing (Figs. 10a and 11a) is generally positive, and shows the largest values in river plume regions, but only during Period II. These are the places where the surface flow responds most directly to the wind. The convergence of tidal pressure work, PW_0, is plotted in Figs. 10b and 11b. We may expect the field to be positive where energy is being lost from the barotropic tide, and this is evident in both the Columbia River estuary and Willapa Bay to the north. It is notably enhanced during the spring tides of Period I. Farther offshore, particularly over Astoria Canyon (directly offshore from the mouth of the CR), there are regions of barotropic pressure work *divergence* (negative convergence), which is a surprising result. It is possible in principle to have barotropic pressure work divergence, e.g. across a stationary hydraulic jump, however the model resolution is not optimized for the slope or canyon, so we have less confidence in results there. The dissipation (Figs. 10c and 11c) is negative definite, and strongest in the estuaries. In Fig. 11c, it is apparent that *DISS* is elevated all across the shelf in Period II relative to Period I, a result of the stronger wind forcing. Buoyancy flux (Fig. 9d) is strongest near the Columbia River mouth, where strong dissipation and stratification coincide. Buoyancy flux is also apparent over Astoria Canyon, as might be expected from the generation of tidal beams.

To understand how the complete energy budget functions over different regions, we will take the volume integral of the tidal average of Eq. (4.14) over larger volumes, encompassing (i) the estuary and (ii) the plume, as shown in Figs. 10d and 11d. The

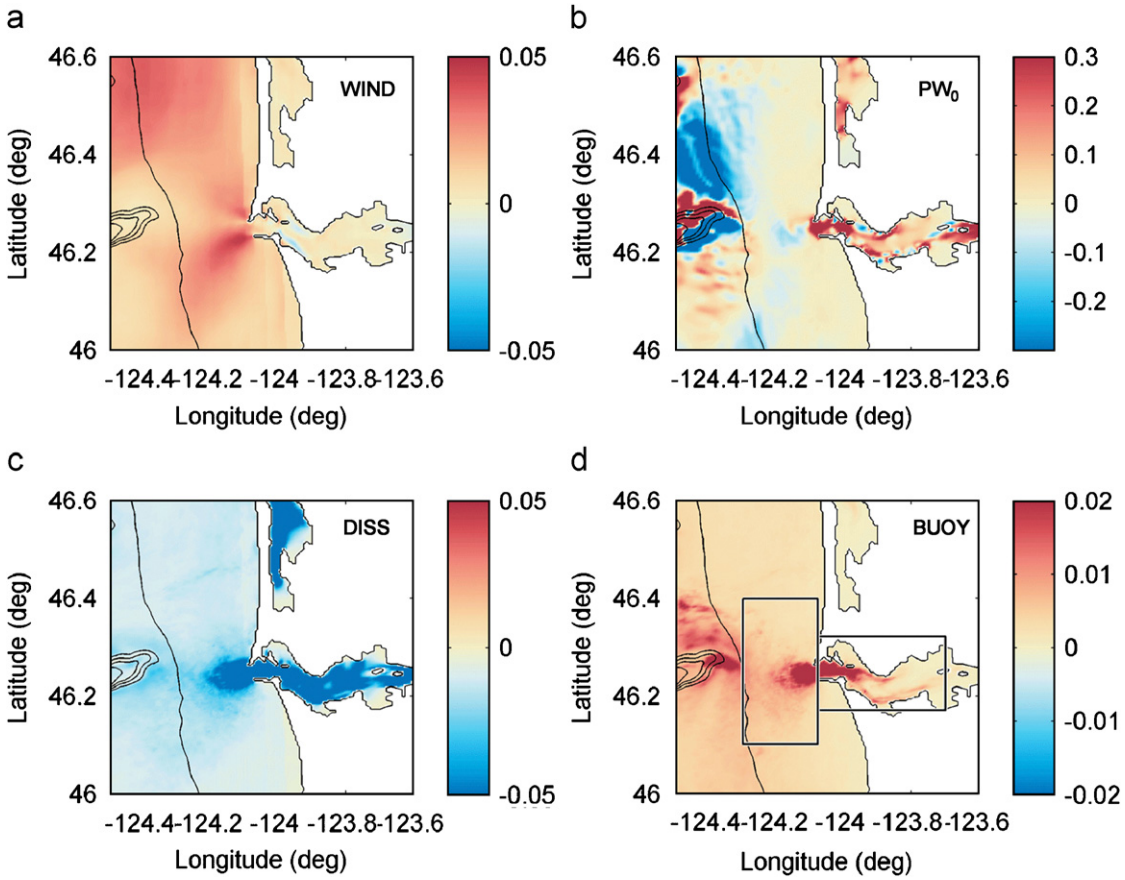

Fig. 11. Selected fields from the time-averaged, vertically integrated, mechanical energy budget, all with units Wm^{-2}. These are averaged over the neap tide, strong upwelling wind Period II indicated in Fig. 2. The wind stress term is plotted in (a). All variable names are as given in (4.14). The tidal pressure work convergence term is plotted in (b). Dissipation and buoyancy flux are plotted in (c) and (d). Isobaths are contoured every 100 m. The "plume" and "estuary" regions for volume integration are indicated by boxes in (d).

resulting values are given in Table 1. The *ERROR* term for each region represents the sum of all terms in Eq. (4.14) if they were moved to the RHS of that equation (and thus should be zero). In general, the error numbers are small compared with the larger forcing terms, but still indicate the need for caution in interpreting these results (especially in the plume volume during Period I). Because of the long averaging period, the storage terms are generally negligible. The tidal pressure work convergence, PW_0, is largest in the estuary (194 MW during Period I) and decreases to just 21 MW in the far field plume in Period I, despite the 15-fold greater volume. These numbers decrease substantially during Period II. Wind is the dominant forcing term in the plume region, but only during Period II, reflecting both the greater surface area and the fact that the thin, buoyant river plume is more likely to develop a current with a downwind component. The net dissipation is strongest in the estuary volume during spring tides (Period I). The difference in forcing mechanisms is evident when we consider where in the water column the dissipation occurs. In the estuary during Period I, two-thirds of the dissipation is in the bottom of the bottom boundary layer, whereas in the plume during Period II it is predominantly higher in the water column, as reflected in $DISS_{INT}$.

The mixing of stratification, *BUOY*, during spring tides is about evenly distributed between estuary and plume, at 5 and 4.6 MW, respectively. The net buoyancy flux drops markedly in the estuary during neap tides, down to 1.6 MW. However, the strong winds in Period II keep *BUOY* in the plume region relatively high, at 3.8 MW (down from 4.6 MW during Period I).

Table 1
Values in megawatts of the tidally-averaged, volume-integrated, terms in the mechanical energy budget (Eq. (4.14)), for the two regions shown in Figs. 10 and 11

Terms in Eq. (4.14) (MW)	Period I: spring tide, weak wind		Period II: neap tide, strong wind	
	Estuary (2.1 km^3)	Plume (30.6 km^3)	Estuary (2.1 km^3)	Plume (30.6 km^3)
KE STORAGE	−0.4	0.0	−0.8	−0.9
PE_0 *STORAGE*	2.9	1.2	0.1	1.4
PE_1 *STORAGE*	0.1	−0.2	−1.2	−3.0
KE ADV	−17.5	9.8	−4.7	−0.3
PE_1 *ADV*	−4.1	6.9	−1.1	−8.9
PW_0	**193.7**	**21.2**	**34.2**	**−1.7**
PW_1	−0.9	10.2	−1.1	9.8
WIND	**−0.3**	**0.8**	**1.1**	**13.1**
$DISS_{INT}$	**−51.9**	**−17.7**	**−11.8**	**−13.7**
$DISS_{BOT}$	**−96.8**	**−21.3**	**−15.4**	**−3.5**
BUOY	**5.0**	**4.6**	**1.6**	**3.8**
ERROR	24.5	13.5	4.8	1.0

Several other terms contribute significantly to the energy budget. In the plume region the advection of PE_1 and the baroclinic pressure work term are both important. The advection of kinetic energy also plays an important role, especially for the plume volume during spring tides. It is beyond the scope of this paper to analyze all of these, but they point to future research questions.

5. Summary and conclusions

In this paper we present results of a realistic numerical hindcast of the Columbia River estuary and plume for the summer of 2004. The model was compared with mooring and CTD data, and was found to have moderate skill as a hindcast.

The tidally averaged, volume-integrated mechanical energy budget of the model was analyzed to determine where and why vertical turbulent buoyancy flux occurred. In terms of forcing, tidal pressure work was greatest in the estuary, whereas either wind or tides were most important in the far field plume, depending on whether it was spring or neap, and on the strength of the wind. While net dissipation, particularly in the bottom boundary layer, was greatest in the estuary, the net buoyancy flux was significant in both the estuary and the plume. This highlights the difficulty of determining net budgets of *BUOY* observationally, because the more dispersed, weaker, and episodic mixing in the wind-driven plume may not be neglected. The mixing efficiency ($BUOY/|DISS|$) is greatest in the plume region, averaging 17% there, whereas it only averages 5% in the estuary. In part, this represents the fact that some of the estuary volume was often unstratified, but it also reflects the fact that the river plume is a stratification feature that is particularly susceptible to wind driven mixing.

Finally, in order to understand the energetics of such a system (or eventually its role in the biological function of a coastal upwelling region), it is clear that we must consider the estuary, plume, and shelf as a single larger system. Only then will we be able to properly tell the story of how deep waters find their way to the surface.

Acknowledgments

This work was generously supported by NSF grant OCE 0239089. The authors would like to sincerely thank the many people who contributed to the ideas and analyses in this paper, including Antonio Baptista, David Darr, Emmanuel di Lorenzo, Mike Foreman, Rob Hetland, David Jay, Steve Lentz, and Scott Tinis. This is RISE contribution #15.

References

Aguilar-Islas, A.M., Bruland, K.W., 2006. Dissolved manganese and silicic acid in the Columbia River plume: a major source to the California Current and coastal waters off Washington and Oregon. Marine Chemistry 101, 233–247.

Allen, J.S., Newberger, P.A., Federiuk, J., 1995. Upwelling circulation on the Oregon Continental Shelf 1. Response to idealized forcing. Journal of Physical Oceanography 25, 1843–1866.

Austin, J.A., Barth, J.A., 2002. Variation in position of the upwelling front on the Oregon shelf. Journal of Geophysical Research 107 (C11), 3180.

Banas, N.S., MacCready, P., Hickey, B.M., 2008. The Columbia River plume as cross-shelf exporter and along-shelf barrier. Continental Shelf Research, this issue, doi:10.1016/j.csr.2008.03.011.

Baptista, A.M., Zhang, Y.L., Chawla, A., Zulauf, M., Seaton, C., Myers III, E.P., Kindle, J., Wilkin, M., Burla, M., Turner, P.J., 2005. A cross-scale model for 3D baroclinic circulation in estuary-plume-shelf systems. II. Application to the Columbia River. Continental Shelf Research 25, 935–972.

Barnes, C.A., Duxbury, A.C., Morse, B.-A., 1972. Circulation and selected properties of the Columbia River Effluent at sea. In: Pruter, A.T., Alverson, D.L. (Eds.), The Columbia River Estuary and Adjacent Ocean Waters. University of Washington Press, Seattle, WA, pp. 41–80.

Barron, C.N., Kara, A.B., Martin, P.J., Rhodes, R.C., Smedstad, L.F., 2006. Formulation, implementation and examination of vertical coordinate choices in the Global Navy Coastal Ocean Model (NCOM). Ocean Modelling 11, 347–375.

Battisti, D.S., Hickey, B.M., 1984. Applications of remote wind forced coastal trapped wave theory to the Oregon and Washington coasts. Journal of Physical Oceanography 14, 887–903.

Beardsley, R.C., Hart, J., 1978. A simple theoretical model for the flow of an estuary onto a continental shelf. Journal of Geophysical Research 83 (C2), 873–884.

Canuto, V.M., Howard, A., Cheng, Y., Dubovikov, M.S., 2001. Ocean turbulence. Part I: One-point closure model—momentum and heat vertical diffusivities. Journal of Physical Oceanography 31, 1413–1426.

Chao, S.-Y., Boicourt, W.C., 1986. Onset of estuarine plumes. Journal of Physical Oceanography 16, 2137–2149.

Chapman, D.C., 1985. Numerical treatment of cross-shelf open boundaries in a barotropic coastal ocean model. Journal of Physical Oceanography 15, 1060–1075.

Divins, D.L., Metzger, D., 2002. NGDC Coastal Relief Model 〈http://www.ngdc.noaa.gov/mgg/coastal/coastal.html〉.

Egbert, G.D., Erofeeva, S.Y., 2002. Efficient inverse modeling of barotropic ocean tides. Journal of Atmospheric and Oceanic Technology 19 (N2), 183–204.

Egbert, G.D., Bennett, A., Foreman, M., 1994. TOPEX/Poseidon tides estimated using a global inverse model. Journal of Geophysical Research 99 (C12), 24,821–24,852.

Emery, W.J., Thomson, R.E., 1997. Data Analysis Methods in Physical Oceanography. Pergamon Press, 634pp.

Fairall, C.W., Bradley, E.F., Rogers, D.P., Edson, J.B., Young, G.S., 1996a. Bulk parameterization of air–sea fluxes for tropical ocean—global atmosphere coupled-ocean atmosphere response experiment. Journal of Geophysical Research 101, 3747–3764.

Fairall, C.W., Bradley, E.F., Godfrey, J.S., Wick, G.A., Edson, J.B., Young, G.S., 1996b. Cool-skin and warm-layer effects on sea surface temperature. Journal of Geophysical Research 101, 1295–1308.

Flather, R.A., 1976. A tidal model of the northwest European continental shelf. Memiores of Society of Royal Science Liege, Series 6 10, 141–164.

Garcia-Berdeal, I., Hickey, B.M., Kawase, M., 2002. Influence of wind stress and ambient flow on a high discharge river plume. Journal of Geophysical Research 107, 13.

Garvine, R.W., 2001. The impact of model configuration in studies of buoyant coastal discharge. Journal of Marine Research 59, 193–225.

Geyer, W.R., Trowbridge, J.H., Bowen, M.M., 2000. The dynamics of a partially mixed estuary. Journal of Physical Oceanography 30, 2035–2048.

Gill, A.E., 1982. Atmosphere–Ocean Dynamics. Academic Press, San Diego, 662pp.

Haidvogel, D.B., 2005. Cross-shelf exchange driven by oscillatory barotropic currents at an idealized coastal canyon. Journal of Physical Oceanography 35 (6), 1054.

Haidvogel, D.B., Arango, H.G., Hedstrom, K., Beckmann, A., Malanotte-Rizzoli, P., Shchepetkin, A.F., 2000. Model evaluation experiments in the North Atlantic Basin: simulations in nonlinear terrain-following coordinates. Dynamics of Atmospheres and Oceans 32, 239–281.

Hickey, B.M., 1998. Coastal oceanography of western North America from the tip of Baja California to Vancouver is. In: Brink, K.H., Robinson, A.R. (Eds.), The Sea, vol. 11. Wiley, pp. 345–393 (Chapter 12).

Hickey, B.M., Pietrafesa, L.J., Jay, D.A., Boicourt, W.C., 1998. The Columbia River plume study. Subtidal variability in the velocity and salinity fields. Journal of Geophysical Research 103, 10,339–10,368.

Hickey, B.M., Geier, S.L., Kachel, N.B., MacFadyen, A., 2005. A bi-directional river plume: the Columbia in summer. Continental Shelf Research 25, 1631–1656.

Hickey, B.M., MacFadyen, A., Cochlan, W.P., Kudela, R.M., Bruland, K.W., Trick, C.R., 2006. Evolution of water properties in the Pacific Northwest in 2005: remote or local wind forcing? Geophysical Research Letters 33.

Hughes, R.P., Rattray, M., 1980. Salt flux and mixing in the Columbia River Estuary. Estuarine and Coastal Marine Science 10, 479–494.

Jay, D.A., Smith, J.D., 1990a. Residual circulation in shallow stratified estuaries. 1. Highly stratified, narrow estuaries. Journal of Geophysical Research 95, 711–731.

Jay, D.A., Smith, J.D., 1990b. Residual circulation in shallow stratified estuaries. 2. Weakly stratified and partially mixed, narrow estuaries. Journal of Geophysical Research 95, 733–748.

Jay, D.A., Smith, J.D., 1990c. Circulation, density distribution and neap-spring transitions in the Columbia River Estuary. Progress in Oceanography 25, 81–112.

Jay, D.A., Smith, J.D., van Leussen, W., 1988. Residual circulation in and classification of shallow, stratified estuaries. In: Dronkers, J. (Ed.), Physical Processes in Estuaries. Springer, pp. 21–41.

Kara, A.B., Barron, C.N., Martin, P.J., Smedstad, L.F., Rhodes, R.C., 2006. Validation of interannual simulations from the 1/8 degree global Navy Coastal Ocean Model (NCOM). Ocean Modelling 11, 376–398.

Kosro, P.M., Peterson, W.T., Hickey, B.M., Shearman, R.K., Price, S.D., 2006. Physical versus biological spring transition: 2005. Geophysical Research Letters 33, L22S03.

Kudela, R.M., Cochlan, W.P., Peterson, T.D., Trick, C.W., 2007. Impacts on phytoplankton biomass and productivity in the Pacific Northwest during the warm ocean conditions of 2005. Geophysical Research Letters 33, L22S06.

Kundu, P.K., Cohen, I.M., 2002. Fluid Mechanics. Academic Press, 730pp.

Landry, M.R., Postel, J.R., Peterson, W.K., Newman, J., 1989. Broad-scale distributional patterns of hydrographic variables on the Washington/Oregon shelf. In: Landry, M., Hickey, B.M. (Eds.), Coastal Oceanography of Washington and Oregon. Elsevier, Amsterdam, pp. 1–40.

Large, W.G., McWilliams, J.C., Doney, S.C., 1994. A review and model with a nonlocal boundary layer parameterization. Reviews of Geophysics 32, 363–403.

Largier, J.L., 1996. Hydrodynamic exchange between San Francisco Bay and the ocean: the role of ocean circulation and stratification. In: Hollibaugh, J.T. (Ed.), San Francisco Bay: The Ecosystem. American Association for the Advancement of Science, pp. 69–105.

Lavelle; J.W., Mofjeld, H.O., Lempriere-Doggett, E., Cannon, G.A., Pashinski, D.J., Cokelet, E.D., Lytle, L., Gill, S., 1988. A multiply-connected channel model of

tides and tidal currents in Puget Sound, Washington and a comparison with updated observations. NOAA Technical Memorandum ERL PMEL-84 (PB89-162515), 103pp.
Li, M., Zhong, L., Boicourt, W.C., 2005. Simulations of Chesapeake Bay estuary: sensitivity to turbulence mixing parameterizations and comparison with observations. Journal of Geophysical Research 110, C12004.
Liu, W.T., Katsaros, K.B., Businger, J.A., 1979. Bulk parameterization of the air-sea exchange of heat and water vapor including the molecular constraints at the interface. Journal of the Atmospheric Sciences 36, 1722–1735.
Lohan, M.C., Bruland, K.W., 2006. Importance of vertical mixing for additional sources of nitrate and iron to surface waters of the Columbia River plume: implications for biology. Marine Chemistry 98, 260–273.
MacCready, P., Hetland, R.D., Geyer, W.R., 2002. Long-term isohaline salt balance in an estuary. Continental Shelf Research 22, 1591–1601.
Marchesiello, P., McWilliams, J.C., Shchepetkin, A., 2001. Open boundary conditions for long-term integration of regional oceanic models. Ocean Modelling 3, 1–20.
Mass, C.F., et al., 2003. Regional environmental prediction over the Pacific Northwest. Bulletin of the American Meteorological Society 84 (10), 1353–1366.
Mellor, G.L., Yamada, T., 1982. Development of a turbulence closure model for geophysical fluid problems. Reviews of Geophysics and Space Physics 20, 851–875.
Munk, W., 1997. Once again: once again—tidal friction. Progress in Oceanography 40 (1), 7–35.
Munk, W., Wunsch, C., 1998. Abyssal recipes II: energetics of tidal and wind mixing. Deep Sea Research Part I: Oceanographic Research Papers 45 (12), 1977–2010.
Nash, J.D., Moum, J.N., 2005. River plumes as a source of large-amplitude internal waves in the coastal ocean. Nature 437, 400–403.
Nash, J.D., Alford, M.H., Kunze, E., 2005. Estimating internal wave energy fluxes in the ocean. Journal of Atmospheric and Oceanic Technology 22, 1151–1570.
Oke, P.R., Allen, J.S., Miller, R.N., Egbert, G.D., Austin, J.A., Barth, J.A., Boyd, T.J., Kosro, P.M., Levine, M.D., 2002. A modeling study of the three-dimensional continental shelf circulation off Oregon. Part I: Model-data comparisons. Journal of Physical Oceanography 32, 1360–1382.
Orton, P.M., Jay, D.A., 2005. Observations at the tidal plume front of a high-volume river outflow. Geophysical Research Letters 32, L11605.
Pan, J., Jay, D.A., Orton, P.M., 2007. Analyses of internal solitary waves generated by the Columbia River Plume with a SAR image. Journal of Geophysical Research 112, C07014.
Peliz, A., Dubert, J., Haidvogel, D.B., 2003. Subinertial response of a density-driven eastern boundary poleward current to wind forcing. Journal of Physical Oceanography 33, 1633–1650.
Simpson, J.H., Brown, J., Matthews, J., Allen, G., 1990. Tidal straining, density currents, and stirring in the control of estuarine stratification. Estuaries 26, 1579–1590.
Stigebrandt, A., Aure, J., 1989. Vertical mixing in the basin waters of fjords. Journal of Physical Oceanography 19, 917–926.
Tinis, S.W., Thomson, R.E., Mass, C.F., Hickey, B.M., 2006. Comparison of MM5 and meteorological buoy winds from British Columbia to Northern California. Atmosphere-Ocean 44, 65–81.
Umlauf, L., Burchard, H., 2003. A generic length-scale equation for geophysical turbulence models. Journal of Marine Research 61, 235–265.
Warner, J.C., Sherwood, C.R., Arango, H.G., Signell, R.P., 2005a. Performance of four turbulence closure models implemented using a generic length scale method. Ocean Modelling 8, 81–113.
Warner, J.C., Geyer, W.R., Lerczak, J.A., 2005b. Numerical modeling of an estuary: a comprehensive skill assessment. Journal of Geophysical Research C5, 2004JC002666.
Weisberg, R.H., Zheng, L., 2003. How estuaries work: a Charlotte Harbor example. Journal of Marine Research 61, 635–657.
Whitney, M.M., Garvine, R.W., 2006. Simulating the Delaware Bay buoyant outflow: comparison with observations. Journal of Physical Oceanography 36, 3–21.
Winters, K.B., Lombard, P.N., Riley, J.J., D'Asaro, E.A., 1995. Available potential energy and mixing in density-stratified fluids. Journal of Fluid Mechanics 289, 115–128.
Wunsch, C., Ferrari, R., 2004. Vertical mixing, energy, and the general circulation of the oceans. Annual Review of Fluid Mechanics 36, 281–314.
Zhong, L., Li, M., 2006. Tidal energy fluxes and dissipation in the Chesapeake Bay. Continental Shelf Research 26, 752–770.
Zhang, Y.L., Baptista, A.M., Myers, E.P., 2004. A cross-scale model for 3D baroclinic circulation in estuary-plume-shelf systems. I. Formulation and skill assessment. Continental Shelf Research 24, 2187–2214.